



Available online at [www.sciencedirect.com](http://www.sciencedirect.com)

ScienceDirect



Journal of Magnesium and Alloys 10 (2022) 1311–1325

[www.elsevier.com/locate/jma](http://www.elsevier.com/locate/jma)

Full Length Article

# Improving the electrochemical stability of AZ31 Mg alloy in a 3.5wt.% NaCl solution *via* the surface functionalization of plasma electrolytic oxidation coating

Mosab Kaseem<sup>a,\*</sup>, Tehseen Zehra<sup>a</sup>, Burak Dikici<sup>b</sup>, Ali Dafali<sup>c</sup>, Hae Woong Yang<sup>d</sup>, Young Gun Ko<sup>e,\*</sup>

<sup>a</sup>Department of Nanotechnology and Advanced Materials Engineering, Sejong University, Seoul 05006, Republic of Korea

<sup>b</sup>Department of Metallurgical and Materials Engineering, Ataturk University, Erzurum 25240, Turkey

<sup>c</sup>Faculty of Sciences Oujda, Department of Chemistry, Mohamed the First University, Oujda, Morocco

<sup>d</sup>Pohang Institute of Metal Industry Advancement, Pohang 37666, Republic of Korea

<sup>e</sup>Materials Electrochemistry Group, School of Materials Science and Engineering, Yeungnam University, Gyeongsan 38541, Republic of Korea

Received 25 May 2021; received in revised form 5 August 2021; accepted 29 August 2021

Available online 6 October 2021

## Abstract

The unique interactions between hexadecanoic acid (HA) and albumin (ALB) molecules on the surface of the porous layer of AZ31 Mg alloy were exploited to fabricate a novel hybrid composite film with excellent electrochemical stability in a 3.5 wt.% NaCl solution. Herein, the inorganic layer (IL) obtained by plasma electrolytic oxidation of AZ31 Mg alloy in an alkaline-phosphate-WO<sub>3</sub> electrolyte was soaked in an organic solution composed of ALB and HA for 10 and 24 h at 60 °C. Although albumin and HA may coexist on the same surface of IL, the higher reactivity of ALB molecules would prevent the formation of a thick layer of HA. The donor-acceptor complexes formed due to the unique interactions between ALB and/or HA and IL surface would reduce the area exposed to the corrosive species which in turn would efficiently protect the substrate from corrosion. The porous structure of the IL would provide preferable sites for the physical and chemical locking triggered by charge-transfer phenomena, leading to the inhomogeneous nucleation and crystal growth of a flowery flakes-like organic layer. DFT calculations were performed to reveal the primary bonding modes between the ALB, HA, and IL and to assess the mechanistic insights into the formation of such novel hybrid composites.

© 2021 Chongqing University. Publishing services provided by Elsevier B.V. on behalf of KeAi Communications Co. Ltd.

This is an open access article under the CC BY-NC-ND license (<http://creativecommons.org/licenses/by-nc-nd/4.0/>)

Peer review under responsibility of Chongqing University

**Keywords:** Hybrid composite; Coordination bond; Albumin; Fatty acid; Porous layer; Corrosion; Theoretical approach.

## 1. Introduction

In recent years, growing interests have been poured into the development of magnesium and its alloys in the automobile and electronic fields due to their lightweight, high strength, and good machinability [1,2]. However, the high corrosion rate of Mg and its alloys would limit the industrial applications of these materials [3]. Therefore, alloying [4] and

surface treatments methods namely chemical conversion coatings, sol-gel, organic/polymer coatings, chemical/physical vapor deposition, anodizing, and plasma electrolytic oxidation (PEO) were suggested by several research groups to improve the protection properties of Mg-based materials in the corrosive environments [5–10]. Among them, PEO has been considered as an environmentally friendly treatment method that leads to form protective oxide layers on the metallic substrates. Briefly, the high voltage applied in an alkaline electrolyte could create numerous micro-sized plasma discharges through a complex process involving thermal, electrochemical, and plasma reactions [11–18]. Since PEO is a surface

\* Corresponding authors.

E-mail addresses: [mosabkaseem@sejong.ac.kr](mailto:mosabkaseem@sejong.ac.kr) (M. Kaseem), [younggun@ynu.ac.kr](mailto:younggun@ynu.ac.kr) (Y.G. Ko).

conversion coating technique, the surface of the metallic alloy is transformed into ceramic *via* electrochemical plasma reactions without damaging the metal alloys at its core. Structures with complex geometries can be coated without distorting the bulk microstructure because the whole substrate does not go through an elevated temperature during PEO coating [4,12]. The plasma discharge activity during PEO would create a porous structure allowing the corrosive species to attack the underlying substrate. Thus, additional treatment would be required to delay or suppress the movement of corrosive species through the defective layer (IL) produced *via* PEO [12].

The application of hydrophobic coatings was proven as an effective approach in inhibiting the corrosion of Mg and its alloys [19]. For example, highly protective hydrophobic coatings can be obtained by using fatty acids that bind to the metallic oxide surfaces through hard acid-hard base interactions in which the metallic cations from the oxide layer acts as hard acid while carboxylate anions from fatty acid behave like hard base [20,21]. Moreover, the long aliphatic chain in these acids would help the development of a highly protective hydrophobic coating [22]. According to Cui et al. [23], the immersion of PEO-coated AZ31 Mg alloy in an ethanolic solution of octadecanoic acid for 10 h would lead to sealing the majority of structural defects of PEO coating where a hydrophobic layer with a contact angle  $\sim 151^\circ$  was obtained through the bonding of  $\text{CH}_3(\text{CH}_2)_{16}\text{COO}^-$  anions to the surface of PEO coating which resulted in significant improvements in the protective properties of the metallic alloy. However, unwanted side reactions would occur during the forming of such hydrophobic coatings because the high electrochemical activity of Mg alloys with many acids, alkalis, and saline solutions would lead to unwanted side reactions [24]. Therefore, the hydrophobic coatings on Mg alloys are not popular when compared to other inert metals, such as Cu, Al, and Ti whose tendency to form passive films on their surfaces [25–27]. Moreover, the chemical activity of Mg alloys is heterogeneous due to the presence of more than two phases with the structure of these materials [18].

On the other hand, novel hybrid materials with various structures could be discovered by hybridization by exploiting the tendency of proteins to interact with a variety of nanomaterials [28]. Thanks to its availability and nontoxicity, albumin (ALB) was utilized to tailor the surface characteristics of IL prepared on Mg alloys. For instance, Kaseem and Ko [29] reported the growth of flowers and rods-like structures on the IL as a result of immersion of IL in solutions containing different concentrations of albumin (ALB) and sodium phosphate which led to forming novel protective composites on the AZ31 Mg alloy. The ALB molecules were used to modify the layered double hydroxide (LDHs) films grown on IL for smart corrosion protection of AZ31 Mg alloy [30]. Although the structural defects of IL can be disadvantages for the corrosion property, they have potential benefits. For example, the large surface area provided by the defect structure would facilitate the self-assembly of organic and inorganic compounds where the local anchoring of these compounds with simple structures around these defects was reported [31].

Based on the discussion above, an issue can be raised of whether it is possible to exploit the competitive interactions between fatty acids and proteins to fabricate an organic layer (OL) on the top of the defective IL to improve the electrochemical stability of the AZ31 Mg alloy substrate. Here, we reported for the first time the formation of novel organic structures on top of the porous surface of IL to fabricate a novel hybrid composite composed of HA-ALB-IL as an individual layer on the surface of AZ31 Mg alloy substrate. The hybrid composite is fabricated by immersing the IL made on Mg alloy *via* PEO in an ethanolic solution containing ALB and hexadecanoic acid (HA). So far, the use of such a defective layer as an immobilization platform for hybrid organic-inorganic flowery structures remains undocumented when two organic compounds were used. The porous surface of IL would play a critical role in providing nucleation sites for self-assembly of ALB-HA which will drive the self-assembly of flowery-like structure. The primary bonding mechanism responsible for flowery structure is proposed based upon DFT calculations of HA and ALB. The effectiveness of the prepared hybrid materials in protecting Mg alloy substrate against corrosion attack was studied and compared with other methods available in the literature.

## 2. Experimental procedures

### 2.1. Fabrication and functionalization of the defective inorganic layer

The material used as a substrate in this study was AZ31 magnesium alloy sheets ( $30 \times 25 \times 4$  mm) with a chemical composition (in wt.%) of 2.89 Al, 0.96 Zn, 0.31 Mn, 0.15 Fe, 0.12 Si, and balance Mg. The AZ31 Mg alloy samples were treated in an electrolyte comprising of 4 g/L KOH, 2 g/L  $\text{WO}_3$ , and 10 g/L of  $\text{Na}_3\text{PO}_4$ . The particle size and zeta potential of  $\text{WO}_3$  were measured to be  $\sim 300$  nm and  $\sim -39$  mV, respectively. Both values were determined by Zetapotentiometer(Nano ZS, ZEN360). The obtained inorganic layer is called IL. The processing parameters, namely oxidation time, current density, and frequency were controlled to be 600 s, 100 mA/cm<sup>2</sup>, and 60 Hz, respectively. To form an OL-IL hybrid composite, the IL samples were functionalized by immersing them in an ethanolic solution (70% ethanol) containing a mixture of 3 g/L albumin (ALB) and (2.5 g/L) hexadecanoic acid (HA) under continuous stirring for 10 and 24 h at 60 °C. The resultant samples were called IL-OL-10 h and IL-OL-24 h, respectively. Based on the preliminary experiments, the immersion periods were selected to be 10 and 24 h because the immersion times below 12 h did not show significant improvement in the corrosion resistance of IL. Whereas the immersion times higher than 24 h caused inferior improvements in the corrosion resistance of the IL sample as compared to the IL sample treated at 24 h. So, we thought the immersion of the IL sample for 24 h in the ALB/HA solution was enough to modify its porous structure.

## 2.2. Microstructural and compositional analysis

The structural morphologies of the examined samples were observed with scanning electron microscopy (SEM-HITACHI, PT-S2800) equipped with dispersive X-ray spectroscopy (EDS). The thickness of the obtained coating was acquired from > 10 different points of at least 5 different cross-sectional morphologies of the samples. The phase compositional analysis of the samples was carried out using X-ray diffraction (XRD; RIGAKU, D-MAX 2500) and X-ray photoelectron spectroscopy (XPS, VG Microtech, ESCA 2000). The Scan range during XRD measurements was from 10 ° to 90 °. The functional groups that appeared due to the post-treatment were analyzed with FTIR-ATR spectroscopy (PerkinElmer Spectrum 100) from a wave-number range of 400–4000 cm<sup>-1</sup>.

## 2.3. Electrochemical analysis

Electrochemical measurements were conducted in an aerated 3.5 wt.% NaCl solution with a potentiostat (Gamry Interface 1000) in a three-electrode configuration, where platinum and Ag/AgCl were set as counter and reference electrodes, respectively. Before potentiodynamic polarization (PDP) measurements, the samples were left in the corrosive solution for 5 h to stabilize the open circuit potential (OCP). PDP curves were scanned from - 0.2 to + 0.4 V versus the OCP at a scanning rate of 1 mV•s<sup>-1</sup>. The Electrochemical impedance spectroscopy (EIS) measurements were performed with AC amplitude of 10 mV over the OCP in the frequency range from 100 kHz to 0.01 Hz after immersion periods of 5, 12, 24, 96, 168, and 336 in the same solution. All electrochemical tests were performed at least four times to ensure data repeatability.

## 2.4. Theoretical calculations

Calculations were performed under the principles of density functional theory (DFT) and the geometry of hexadecanoic acid (HA) and albumin (ALB) molecules was optimized via the B3LYP/6-311G(d,p) basis set using the Gaussian (09) software [32–34]. The reactivity of ALB and HA molecules was examined by calculations of the energy of the highest occupied molecular orbital ( $E_{HOMO}$ ) as well as the energy of the highest occupied molecular orbital ( $E_{LUMO}$ ). The values of energy gap ( $\Delta E_{gap}$ ), dipole moment ( $\mu$ ), ionization potential ( $I$ ), electron affinity ( $A$ ), Mulliken's electronegativity ( $\chi$ ), absolute hardness ( $\eta$ ) and absolute softness ( $S$ ) were estimated by following equations [31]:

$$I = -E_{HOMO} \quad (1)$$

$$A = -E_{LUMO} \quad (2)$$

$$\chi = \frac{I + A}{2} \quad (3)$$

$$\eta = \frac{I - A}{2} \quad (4)$$

$$S = \frac{1}{\eta} \quad (5)$$

The fraction of emitted electrons ( $\Delta N$ ) was calculated using the above formula [31]:

$$\Delta N = \frac{(\chi_{Mg} - \chi_{mol})}{2(\eta_{Mg} + \eta_{mol})} \quad (6)$$

Here,  $\chi_{Mg}$  and  $\eta_{Mg}$  represent the theoretical value of Mulliken's electronegativity and hardness value of Mg, respectively, while  $\chi_{mol}$  and  $\eta_{mol}$  are the calculated electronegativities and hardness values of organic molecule respectively. The theoretical values of  $\chi_{Mg}$  and  $\eta_{Mg}$  for Mg are found to be 3.75 eV mol<sup>-1</sup> and 3.90 eV mol<sup>-1</sup>, respectively [35].

## 3. Results and discussion

### 3.1. . Microstructure of hybrid composites

**Fig. 1(a–c)** shows the surface morphologies of IL, IL-OL-10 h, and IL-OL-24 h samples before and after the post-treatment using an organic solution containing HA and ALB. As shown in **Fig. 1a**, the surface of IL reveals micropores with a multi-level layout. The hyper-level pores show an irregular, pit-like shape, while their hypo-level counterparts show a circular shape. These multi-level micropores arise due to the plasma discharge activity during PEO [12, 36–38]. Cracks highlighted by arrows in **Fig. 1a** are attributed to the residual thermal stress generated within the IL as a result of the rapid solidification of molten materials by the cold electrolyte [39]. In contrast, multi-level pores observed on the surface of the IL sample became less dominant on the surface of IL-OL-10 h and IL-OL-24 h samples. After the post-treatment process in a solution of HA and ALB, the nucleation of flowery flakes on top of the IL surface was started as shown in **Fig. 1b** for the IL-OL-10 h sample. The large surface area provided by IL due to the presence of micropores would responsible for such nucleation of flowery flakes like agglomerates of HA-ALB (OL) on the surface of IL. Accordingly, the structural defects that exist on the IL surface before the post-treatment are sealed due to the growth flowery-flake structure as shown in **Fig. 1 (b–e)**. Such effective sealing would be attributed to the unique interactions between the ALB and HA on the surface of IL which lead to an anisotropic growth of primary clusters by self-assembly [12,13,21]. The active adsorption of OL (HA-ALB) operating the growth process is affected by the porous structure of IL and the bonding compatibility between IL and OL by electron donor-acceptor reactions, as we will be approved later by DFT calculations. Thus, ALB and/or HA molecules would provide electrons to the solution and the porous IL surface leading to the formation of the hybrid organic-inorganic film. EDS mappings on the surface of OL-IL-10 h indicated the existence of Mg, O, P, W, C,

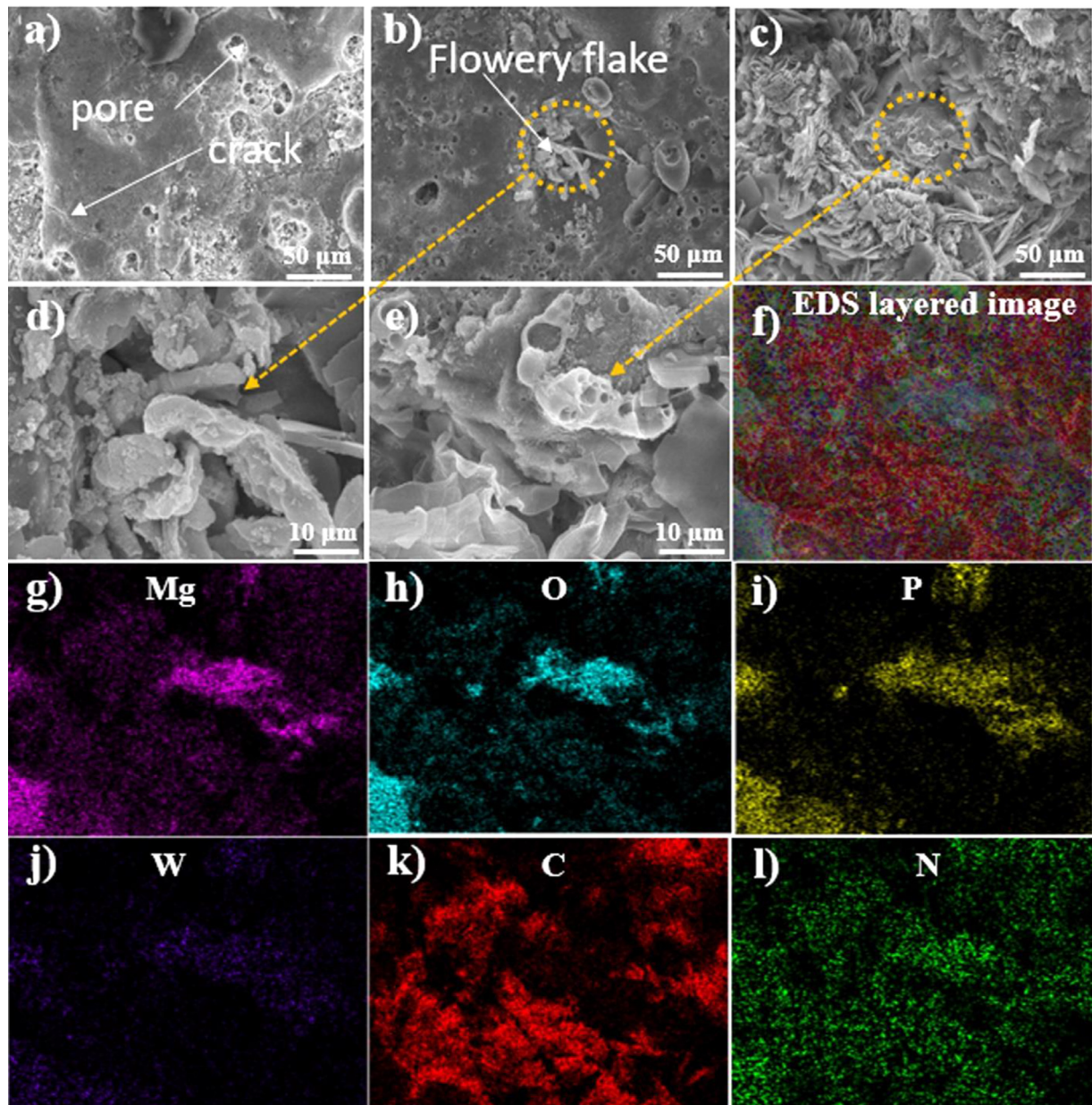


Fig. 1. (a–e) SEM images showing the surface morphologies of the samples (a) IL, (b and d) IL-OL-10 h, (c and e) IL-OL-24 h. (f–n) EDS mapping analysis on the surface of IL-OL-24 h sample shown in Fig. 1c where the Mg, O, P, W, C, and N elements were detected.

Table 1  
EDS analysis on the surface of IL, IL-OL-10 h, and IL-OL-24 h samples.

Sample	Mg (wt.%)	O (wt.%)	P (wt.%)	W (wt.%)	C(wt.%)	N (wt.%)
IL	35.34	40.58	18.79	5.29	–	–
IL-OL-10h	27.14	36.16	9.67	4.23	21.53	1.27
IL-OL-24h	25.27	29.01	7.56	4.11	30.76	3.29

and N elements which tended to distribute homogeneously throughout the surface of the hybrid film. The presence of C and N would confirm the active adsorption of the OL on the surface of IL. The EDS elemental composition on the surface of IL, IL-OL-10 h, and IL-OL-24 h samples (Table 1) shows the contents of the elements that appeared in EDS mappings shown in Fig. 1(f–n).

Fig. 2 (a–c) displays the corresponding cross-sectional images of the IL, IL-OL-10 h, and IL-OL-24 h. The thickness of the hybrid composites was found to be  $\sim 23.2$  and  $\sim 24.3$   $\mu\text{m}$  for IL-OL-10 h and IL-OL-24 h samples, respectively while the thickness of IL was calculated to be  $\sim 20.1$   $\mu\text{m}$ . As indicated by yellow circles, the formation of flowery flakes led to the sealing of micro-pores in IL-OL-10 h and IL-OL-24 h

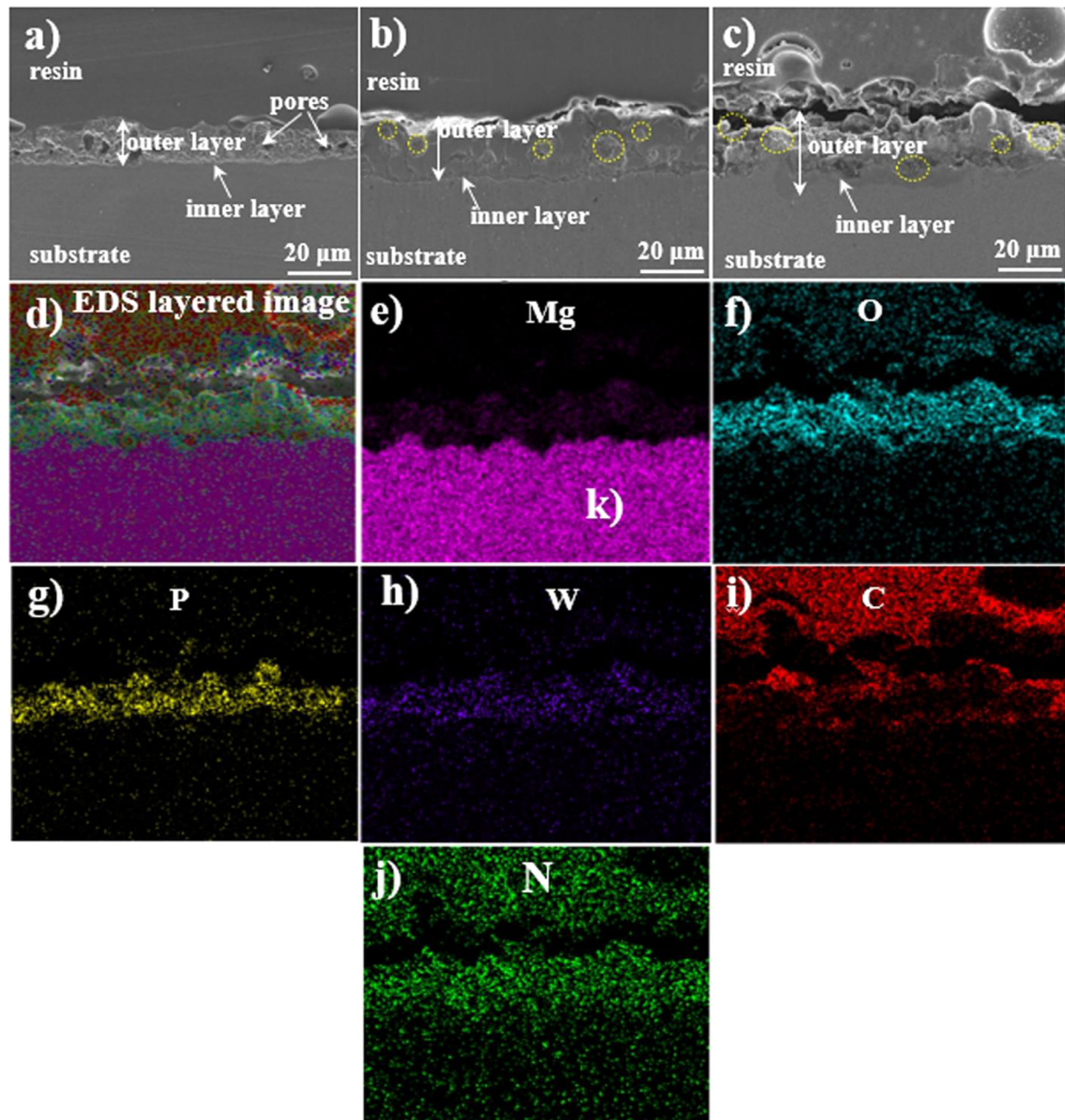


Fig. 2. (a–c) SEM images showing the cross-sectional morphologies of (a) IL, (b) IL-OL-10 h, (c) IL-OL-24 h. (d–j) The corresponding EDS mapping of the IL-OL-24 h sample showing the presence of Mg, O, P, W, C, and N elements (For interpretation of the references to color in this figure, the reader is referred to the web version of this article).

samples. The EDS elemental mappings, shown in Fig. 2 (d–j), confirmed the existence of Mg, O, P, W, N, and C in the sealed porous structure.

### 3.2. Compositional analysis of hybrid composites

Fig. 3(a) displays the FT-IR spectra of IL-OL-10 h, and IL-OL-24 h to prove the interaction of PA and ALB with IL. The peaks evident at  $\sim 1520\text{ cm}^{-1}$  and  $\sim 1573\text{ cm}^{-1}$  are attributed to  $-\text{COO}^-$  asymmetric and symmetric stretching vibrations, respectively; though according to Liu et al. [22], the symmet-

ric stretching peak of  $-\text{COO}^-$  should be at  $\sim 1468\text{ cm}^{-1}$  which suggested that a combination of different interactions would occur on the surface of IL. Similar findings were reported by Cui et al. [23] who examined the sealing effect of AZ31 Mg alloy by stearic acid. The peaks at  $\sim 1022\text{ cm}^{-1}$  would be attributed to the ethanol adsorbed on the surface [23]. The peaks at about  $2867$  and  $2943\text{ cm}^{-1}$  were contributed to the C–H asymmetric and symmetric stretching vibration, respectively [40]. The position of the N–CO–NH<sub>2</sub> group in ALB is commonly used to discover the conformational changes on the ALB molecule during the adsorption on the metallic sur-

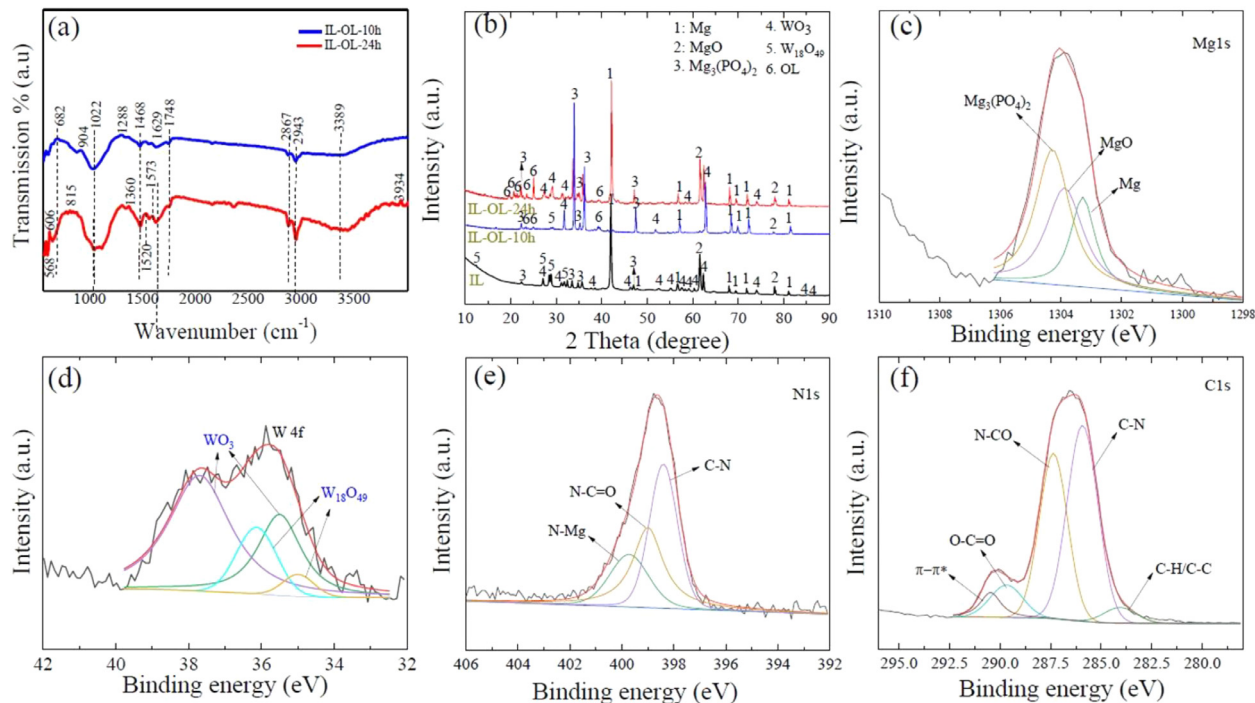


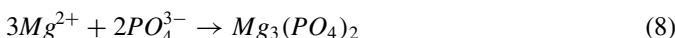
Fig. 3. (a) FTIR spectra of IL, IL-OL-10 h, and IL-OL-24 h samples. (b) XRD analysis of the IL, IL-OL-10 h, and IL-OL-24 h samples. (c–f) The high-resolution scan for (c) Mg 1 s, (d) W 4f, (e) C 1 s, and (f) N 1 s for IL-OL-24 h sample.

face [41,42]. In this work, the N–CO–NH<sub>2</sub> group vibrations were noticed at 1686 and 1645 cm<sup>-1</sup> which is slightly different from the values of the amide group reported of pure ALB which usually occurs at 1629–1748 cm<sup>-1</sup> [41]. This change in band position suggested that interaction with ALB with IL and HA surface would induce strong changes in ALB conformational state in favor of less-ordered conformations. The band at 1520 cm<sup>-1</sup> would be related to an interaction between NH<sub>2</sub> and positively charged sites (Mg sites) on the IL surface [21].

The compositional analyses of IL, IL-OL-10 h, and IL-OL-24 h samples were investigated by XRD, as shown in Fig. 3b. MgO, Mg<sub>3</sub>(PO<sub>4</sub>)<sub>2</sub>, WO<sub>3</sub>, W<sub>18</sub>O<sub>49</sub>, and Mg were detected in the IL sample. MgO can be formed by the Mg<sup>2+</sup> generated from AZ31 Mg alloy substrate and O<sup>2-</sup> anions produced from the electrolyte during PEO (Eq. (7)):



PO<sub>4</sub><sup>3-</sup> anions produced from the ionization of Na<sub>3</sub>PO<sub>4</sub> are moved toward the anode under the effect of the high electric field and react with Mg<sup>2+</sup> cations in the vicinity of the anode (Eq. (8)):



The peaks of Mg were detected due to the penetration of X-rays into the AZ31 Mg alloy substrate through the porous thin layer. The presence of WO<sub>3</sub> and W<sub>18</sub>O<sub>49</sub> is ascribed to the successful incorporation of the WO<sub>3</sub> additive, and its transformation to W<sub>18</sub>O<sub>49</sub> under plasma conditions [31]. Since WO<sub>3</sub> nanoparticles possessed a negative zeta potential, their electrophoretic movement towards the anode would ensure

the delivery of the particles at the anode-electrolyte interface [11,12]. Thus, the incorporation of these nanoparticles during the PEO process could occur by the electrophoresis process, then the high local temperature of plasma discharges melted and sintered the WO<sub>3</sub> nanoparticles into the coating [12]. Here, two assumptions were considered to be important during the incorporation behavior of WO<sub>3</sub> nanoparticles *via* the PEO process. First, the extent of oxygen evolution during the initial stages of the PEO process could be helpful to determine the preservation of these particles that are already embedded in the solution. Second, the breakdown phenomena of the coating and generation micro-pores and cracks could decide the migration of WO<sub>3</sub> nanoparticles at the later stages of the PEO process. The high plasma temperature during PEO would facilitate the phase transformation of WO<sub>3</sub> to W<sub>18</sub>O<sub>49</sub> [31]. On the other hand, the XRD patterns of OL-IL-10 h and OL-IL-24 h samples showed the additional peaks at 20.01, 20.76, 21.50, 23.57, and 39.41° along with their observed peaks of IL, suggesting the successful formation of OL on the top of IL. The complete growth of the flowery flakes which seal the entire porous structure in the case of the IL-OL-24 h sample would explain the high intensity of these peaks in comparison to the case of the IL-OL-10 h sample.

The chemical states of the flowery-flake structures are investigated in detail by XPS analysis. Fig. 3 (c–f) shows the high-resolution spectra of Mg 1s, W 4f, C 1s, and N 1s for the IL-OL-24 h sample. The deconvolution of the Mg 1s spectrum led to three peaks at binding energies of ~1303.28 eV, ~1303.88 eV, and ~1304.28 eV corresponded to Mg, MgO, and Mg<sub>3</sub>(PO<sub>4</sub>)<sub>2</sub> respectively [31]. The spectrum W 4f was decomposed into peaks of W 4f<sub>7/2</sub>, and W 4f<sub>5/2</sub> for IL, where the

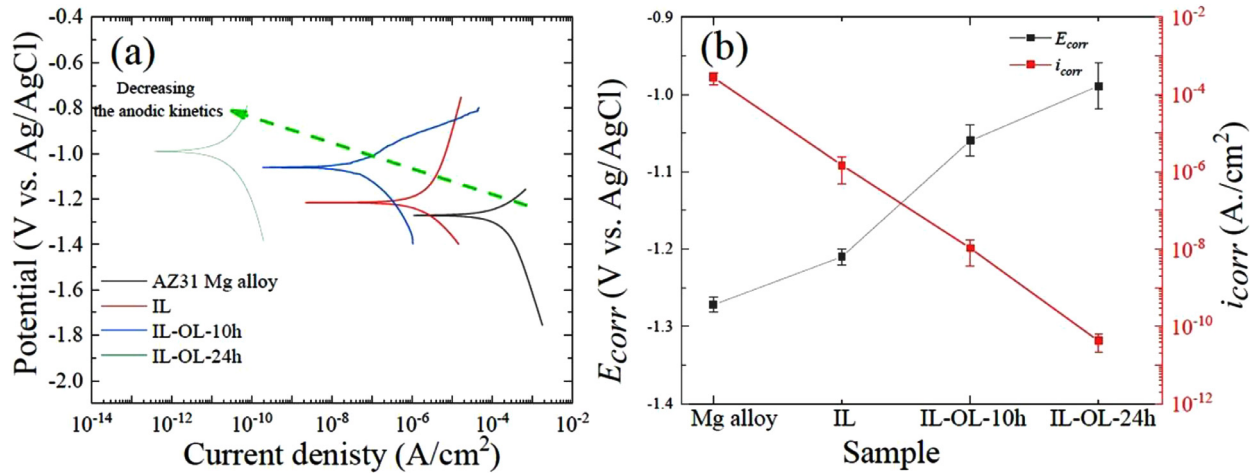


Fig. 4. (a) PDP curves scanned from - 0.25 to + 0.40 V concerning the OCP at a scan rate of 1 mV/s for AZ31 Mg alloy, IL, IL-OL-10 h, and IL-OL-24 h samples. (b)  $E_{corr}$  vs.  $i_{corr}$  for AZ31 Mg alloy, IL, IL-OL-10 h, and IL-OL-24 h samples.

binding energy at  $\sim 34.38$  eV and  $\sim 36.5$  eV associated with  $W_{18}O_{49}$ , and the binding energies at 35.48 eV, and 37.75 eV corresponded to  $WO_3$  [31]. The deconvolution of the N 1s spectrum shows three deconvoluted peaks at  $\sim 398.4$  eV representing C–N bond, and at  $\sim 399.2$  eV representing N–C = O group, and at  $\sim 399.8$  eV describing the N–Mg bond, suggesting the binding of Mg with ALB to form coordinating complexes [31]. As such, the deconvolution of C 1s spectrum showed five peaks at  $\sim 284$  eV,  $\sim 285.7$  eV,  $\sim 287.3$  eV,  $\sim 289.4$  eV, and  $\sim 290.4$  eV related to (C–C/C–H), (C–N), and (N–C = O), (O–C = O), and  $\pi$ - $\pi$  respectively [19, 43–45]. The detection of the C 1s and N 1s peaks, arising from the post-treatment in a solution composed of ALB and HA, would suggest the adsorption of ALB and HA on the surface of IL, forming flower-like organic structures.

### 3.3. Electrochemical performance of hybrid composites

**Fig. 4a** shows PDP curves of the AZ31 Mg alloy substrate, IL, IL-OL-10 h, and IL-OL-24 h samples with a direct comparison with the IL before the post-treatments in a solution of ALB and HA. The parameters of corrosion current density ( $i_{corr}$ ) and corrosion potential extracted from PDP curves are plotted in **Fig. 4b**. As shown in **Fig. 4b**, the AZ31 Mg alloy substrate had a higher corrosion susceptibility as compared to other samples which was reflected by the largest value of  $i_{corr}$  and the most negative value of  $E_{corr}$ . Although the PEO coating (IL sample) led to improve the corrosion resistance of the AZ31 Mg alloy, the formation of flowery structures on the surface of IL-OL-10 h and IL-OL-24 h samples resulted in significant changes in terms of the  $E_{corr}$  and  $i_{corr}$  which correlate with the thermodynamics and kinetics of the corrosion reactions, respectively. As shown in **Fig. 4a**, the PDP curve of the IL sample was shifted to the nobler potential after deposition of the OL layer where the most positive increase in the potential was observed in the IL-OL-

24 h sample. This is attributed to the sealing of structural defects of IL by the OL, limiting the activity of the whole surface. Therefore, its surface becomes less prone to chemical processes, as indicated by the noble shift of  $E_{corr}$ . The PDP curves of IL-OL-10 h and IL-OL-24 h samples showed a shift to the lower region of the  $i_{corr}$ , which indicates slower anodic reactions. This result suggests that the flowery-flakes structure is an effective approach to improve the stability of IL by blocking the porous structure and improving the barrier properties. In other words, the flowery-like structures can be considered as a potential candidate to improve the durability of anti-corrosion layers by sealing the structural defects and strengthening the barrier properties. This would, in turn, block the additional inward flow of the corrosive ions ( $Cl^-$ ) into the substrate. Moreover, such structures would provide additional shielding that prevented the flow of the corrosive ions towards the multi-level micropores. Therefore, it is believed that the high stability in the corrosive solution of the IL-OL-24 h sample is attributed to the complete and uniform sealing of micro-pores due to the deposition of OL acting as a barrier film.

**Fig. 5(a–c)** shows the cross-sectional images of IL, IL-OL-10 h, and IL-OL-24 h samples after 5 h immersion in a 3.5 wt.% NaCl solution. It can be seen from **Fig. 5a** that IL had suffered severe corrosion since many corroded areas were found on the surface of this sample. In contrast, the flake-like structure in IL-OL-10 h and IL-OL-24 h samples film protected the Mg alloy substrate to some extent where some degraded areas are rarely observed, as shown in **Fig. 5** (b and c). Interestingly, the cross-sectional image of the IL-OL-24 h sample (**Fig. 5c**) was almost unaffected by the corrosion, confirming that the effectiveness of the flower-flakes structure in improving the protection properties of AZ31 Mg alloy substrate.

To approve the effectiveness of the approach proposed in the present work, the  $i_{corr}$  and  $E_{corr}$  values derived from PDP tests were compared with data in the literature as displayed

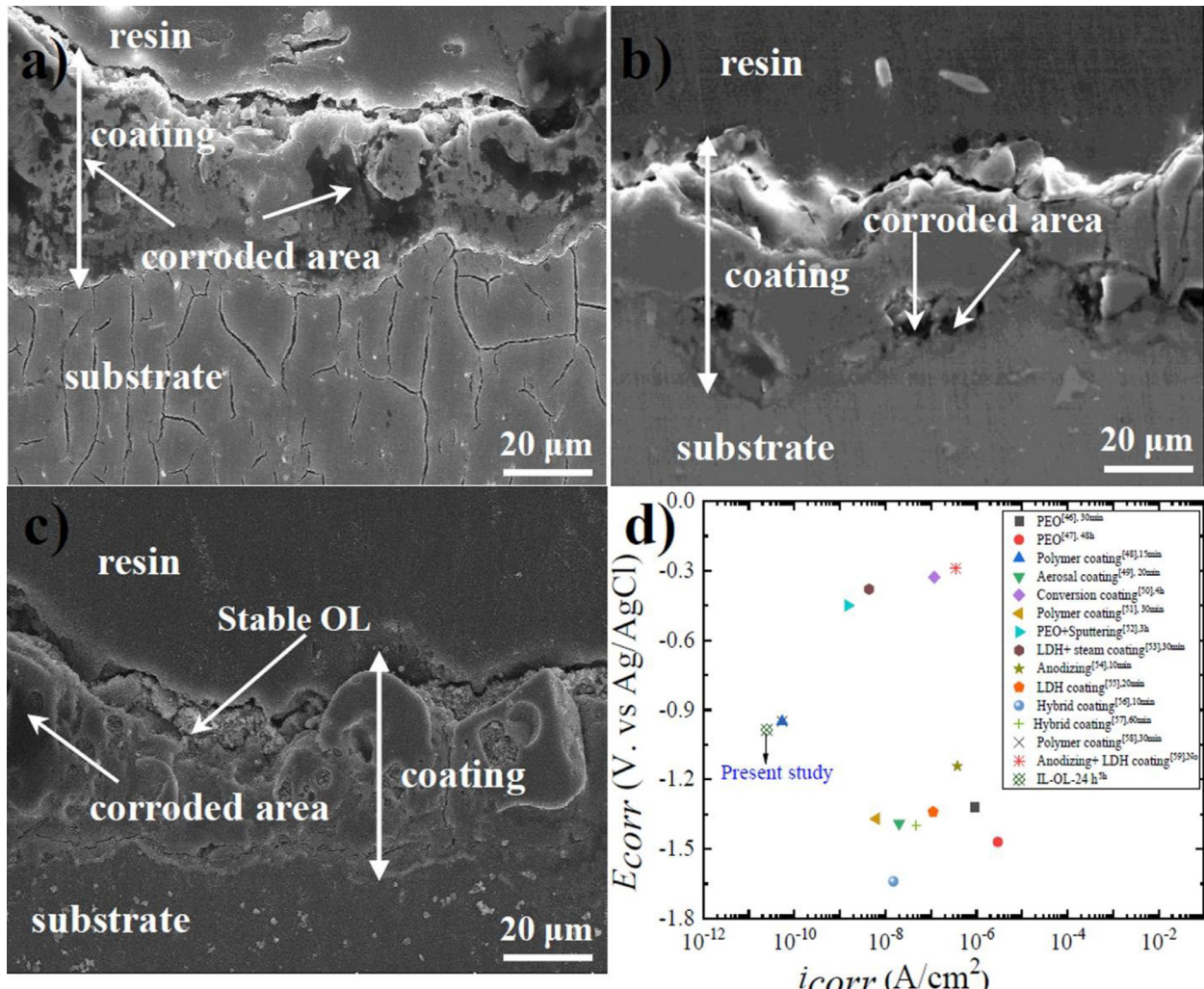


Fig. 5. (a–c) Morphological features of the samples after 5 h immersion in 3.5 wt.% NaCl solution where (a) IL sample, (b) IL-OL-10 h sample, and (c) IL-OL-24 h sample. (d) Comparison of  $E_{corr}$  and  $i_{corr}$  values obtained in the present work with the counterparts values collected for Mg alloy substrates treated by couples of surface treatments [46–59]. The immersion periods in the corrosive solutions were varied from 10 min to 5 h.

in Fig. 5d. For the examples shown in Fig. 5d, the immersion times before PDP tests were varied from 10 min to 4 h. As it can be seen from Fig. 5d, the formation of flowery flakes structures on the surface of IL, through the unique interactions between ALB and HA molecules, is an effective method to improve the protection properties of Mg substrates in comparison to different PEO coatings, conversion coatings, LDH coating, anodizing, hybrid coating, and anodizing+LDH coatings [46–59]. Although the value of  $E_{corr}$  of the IL-OL-24 h sample was more negative than the other cases, the smallest value of  $i_{corr}$  ( $2.47 \times 10^{-11} A/cm^2$ ) for this sample would imply a superior corrosion resistance of the AZ31 Mg alloy in comparison to the literature data. This was attributed to the stable barrier protection achieved by flowery flakes structures formed due to the unique interactions between ALB and HA on the surface of IL. Even a longer immersion period of 5 h was used in the present work, better corrosion resistance was obtained in comparison to other studies shown in Fig. 5d in which the samples were immersed in the corrosive solutions

for shorter periods (from 10 min to 4 h). Since all materials employed in the present works were almost less toxic and eco-friendly, the present approach can be applied to fabricate functional hybrid composites with potential biomedical applications.

#### 3.4. EIS evaluation for long time immersion

For the assessment of the corrosion performance of the coatings with prolonged exposition to 3.5 wt.% of NaCl solution, EIS measurements were performed at different immersion times up to 336 h. The results obtained for the IL, IL-OL-10 h, IL-OL-24 h samples are presented in Fig. 6, in the form of Nyquist and Bode plots. Regardless of the immersion time, the IL sample showed lower corrosion resistance than IL-OL-10 h and IL-OL-24 h samples as deduced from the smaller diameter of the capacitive loops in the Nyquist plots and the lower values of modulus of impedance at low frequencies. As the immersion time increase, IL exposes to the

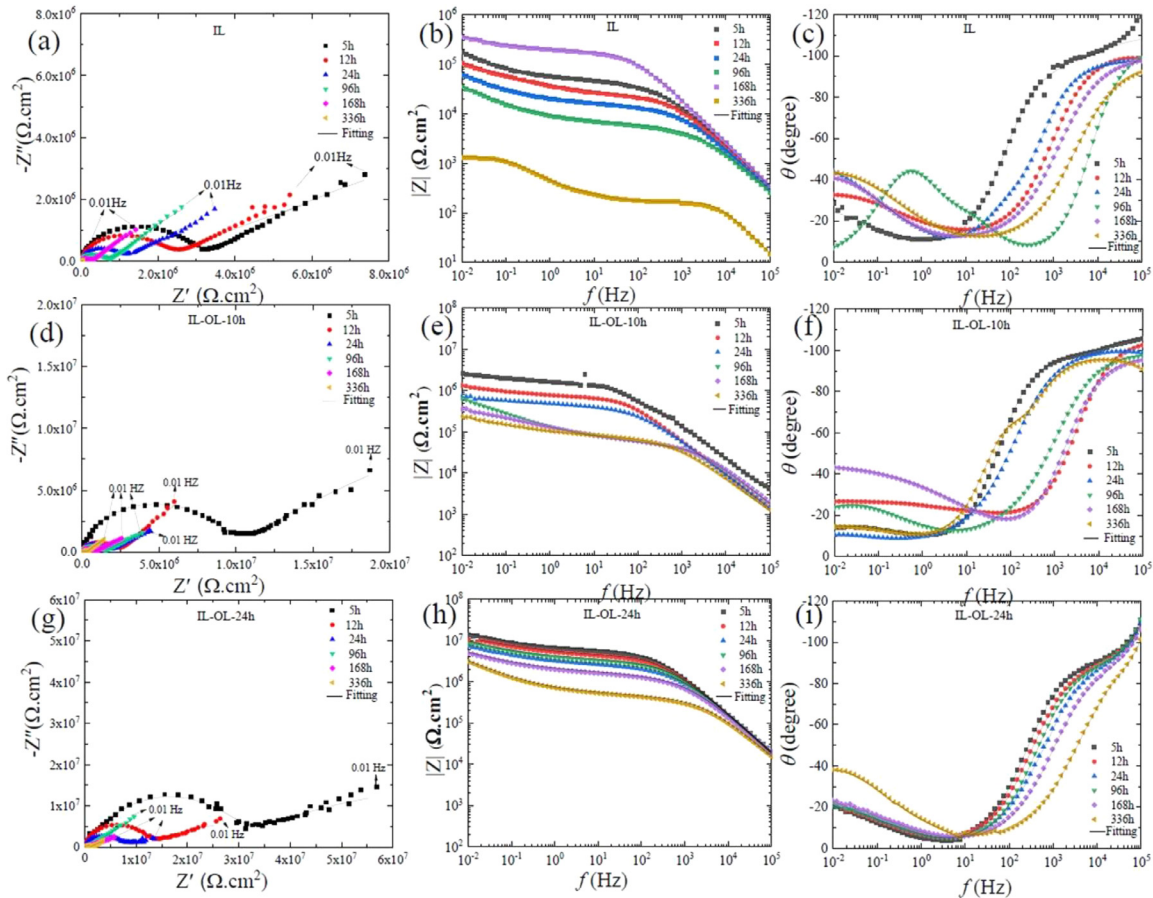


Fig. 6. EIS results obtained for the IL, IL-OL-10 h, and IL-OL-24 h samples at different immersion times, where (a–c) IL sample, (d–f) IL-OL-10 h sample, and (g–i) IL-OL-24 h sample. The solid lines represent the fitting curves obtained with the equivalent circuits.

corrosive media and form loose  $\text{Mg}(\text{OH})_2$  [60], which has no blocking effect on  $\text{Cl}^-$ , thus facilitating a further degradation during 12–168 h immersion. This degradation became more pronounced when the immersion time reaches 336 h where the diameter of the capacitance loop of IL diminished significantly. The significant shrink of capacitive loops and drop of the total impedance of IL sample with increasing immersion time confirm the less protection of the coating and the active dissolution of the IL sample. The defects in the IL sample (micropores and microcracks) acted as the active sites, providing pathways for quick diffusion of corrosive ions to the substrate with a higher corrosion rate. With increasing immersion time up to 368 h, the large drop of corrosion resistance would imply that the substrate had been corroded seriously because of the insufficient protection. Although the diameters of the capacitive loops in the Nyquist plots for IL-OL-10 h and IL-OL-24 h samples were reduced with increasing the immersion times, the corrosion resistance of these samples was higher than that for the IL sample, which can be considered as sealing effect, and shows a slow-corrosion process during long-term immersion.

In general, the EIS spectrum in a broad frequency range may exhibit one, two, or more time constants depending on whether the coating has a single-layered or multi-layered

structure, whether it is porous or compact, whether the space-charge region that puts restrictions on the charge transfer forms at the potential used, or the charge transfer process is effected by diffusion [61]. The impedance response for the three samples at different immersion periods indicates the presence of several relaxation processes, as revealed by phase plots in Fig. 6 (c,f,i). At least two-time constants for IL, IL-OL-10 h, and IL-OL-24 h samples can be identified from the phase angle plots shown in Fig. 6 (c,f,i). It is also evident that the IL-OL-10 h and IL-OL-24 h samples had higher phase angle values corresponding to the higher frequency (1 MHz) as compared to the IL, suggesting higher corrosion protective ability. Moreover, it can be seen some deviation of the phase maximum values from  $90^\circ$  which indicates a non-ideal capacitor behavior. Lopez-Ortega et al. [62], attributed this dispersion to inhomogeneities in the dielectric material, *i.e.* passive layer, such as porosity, mass transport, and the relaxation effect. The time constants, however, are hardly observed due to a strong overlying [63,64]. Similar findings were reported by Zhang et al. [65] and Kaseem et al. [13] for the PEO coating made on AZ31 Mg alloy followed by several types of post-treatments. The protective properties can be measured from the value of  $|Z|_{f \rightarrow 0}$  in the modulus Bode plots [66,67]. As shown in Fig. 6 (b, e, h), the high values of  $|Z|_{0.1 \text{ Hz}}$  can

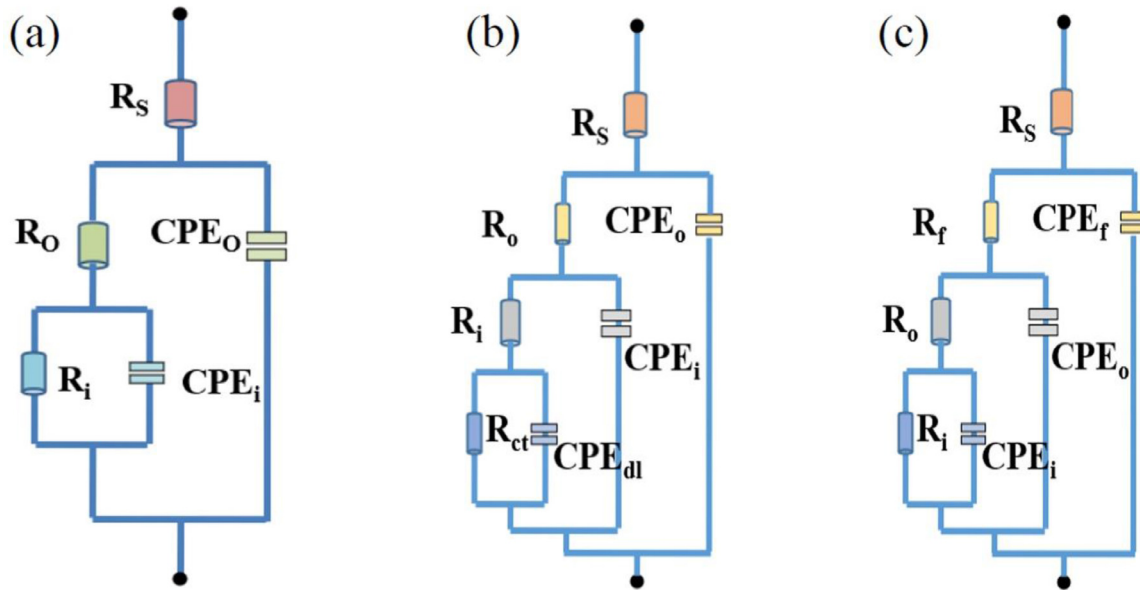


Fig. 7. (a) The equivalent circuit model used for fitting the EIS results of the IL sample at immersion periods up to 96 h. (b) The equivalent circuit model used for fitting the EIS results of IL sample at immersion periods of 168 and 336 h. (c) The equivalent circuit model used for fitting the EIS results of IL-OL-10 h, and IL-OL-24 h samples.

clearly present the beneficial effect of immersion in an organic solution composed of ALB and HA for all immersion times. Interestingly, the values of  $|Z|_{0.1 \text{ Hz}}$  for the IL-OL-24 h sample were significantly higher than other cases which would confirm that the flowery flake structures could significantly suppress the movement of corrosion species towards metallic alloy substrate, which was consistent with the PDP results.

To explore the different electrochemical processes that the hybrid composite films undergo, the impedance responses are fitted to equivalent circuit (EC) models shown in Fig. 7 by considering the physical and chemical features. Due to the dual-layered structure of the IL sample, two constant phase elements, such as  $CPE_o$  and  $CPE_i$  corresponded to the outer layer and the inner layer, respectively were used. Here,  $R_o$  describes the resistance of the outer layer while  $R_i$  indicates the resistance of the inner layer. Therefore, the EC model shown in Fig. 7a was used for fitting EIS results of the IL sample at immersion times up to 96 h while the EC model in Fig. 7b was used for fitting the results at longer immersion periods of 168 and 336 h. Here,  $CPE_{dl}$  and  $R_{ct}$  describe the double-layer capacitance and charge transfer resistance at the Mg alloy/solution interface. As for IL-OL-10 h and IL-OL-24 h samples, the EC model in Fig. 7c was used for fitting the EIS results. In this model,  $CPE_f$  and  $R_f$  represented the constant phase element and the resistance of the flowery flakes grown on the surface of IL. The pure capacitor was replaced with a  $CPE$  owing to the inhomogeneous surface of the coatings obtained via PEO [68]. The chi-squared ( $\chi^2$ ) error value was  $10^{-3}$  order of magnitude for all cases, implying that the EC models in Fig. 7 were adequate for fitting Fig. 6. The parameter values drawn from these equivalent circuit models are available in Tables 2–4. In all samples, the values of  $R_i$

were higher than values of  $R_o$  due to the compact structure of the coatings produced via PEO [12]. In addition to the high values of  $R_o$  and  $R_i$  in comparison to that of the IL sample, the higher protective ability provided by IL-OL-10 h and IL-OL-24 h samples would be reflected by the presence of  $R_f$ . It can be noted that the IL-OL-24 h samples showed the highest values of the  $R_f$  and  $R_o$  for all times of immersion. The evolution of the  $R_i$  for the three samples after different immersion periods in a 3.5 wt.% NaCl solution revealed that the values of  $R_i$  were almost identical for samples at short immersion periods (5 and 12 h) in a 3.5 wt.% NaCl solution. Although the values of  $R_i$  showed a sharp decrease with increasing immersion times, the values of  $R_i$  for IL-OL-24 h were almost unchanged by increasing the immersion time, indicating considerable corrosion protection of the inner layer of the IL sample was obtained by the deposition of OL which has flowery flake structure.

The physical meaning of  $CPE$ 's parameters would be correlated with the morphology of the IL, IL-OL-10 h, and IL-OL-24 h samples. The high value of  $CPE-Y$  value for the IL sample would suggest that a larger surface area would be exposed to the 3.5 wt.% NaCl solution, facilitating the charge transfer of  $\text{Cl}^-$  species towards the AZ31Mg alloy substrate [69]. In contrast, the low values of the  $CPE_f$  for the IL-OL-24 h sample would be an indicator of the effective suppression of the infiltration of corrosive ions due to the formation of flowery flakes structure, covering the entire porous surface of IL. On the other hand, the values of  $CPE-n$  would describe the uniformity of each sample where the high values of  $CPE-n_f$  in the IL-OL-24 h sample would reflect the high uniformity of this sample which led to reduce the exposed interfacial surface, impeding anodic dissolution of AZ31 Mg alloy [12,70].

Table 2

Electrochemical parameters obtained from fitting IL sample. The unit of Y is ( $\text{S} \cdot \text{s}^n \cdot \text{cm}^{-2}$ ) while the unit of R is ( $\Omega \text{ cm}^2$ ).

Period (h)	$CPE_o$		$R_o$	$CPE_i$		$R_i$	$CPE_{dl}$		$R_{ct}$	$\chi^2 (\times 10^{-3})$
	$Y_0$	$n_o$		$Y_i$	$n_i$		$Y_{ct}$	$n_{ct}$		
5	$1.38 \times 10^{-11}$	0.92	$4.88 \times 10^6$	$1.44 \times 10^{-10}$	0.72	$6.53 \times 10^7$	—	—	—	1.69
12	$7.19 \times 10^{-11}$	0.89	$1.60 \times 10^6$	$5.88 \times 10^{-10}$	0.90	$4.97 \times 10^7$	—	—	—	2.81
24	$3.90 \times 10^{-11}$	0.88	$8.15 \times 10^5$	$6.83 \times 10^{-8}$	0.27	$1.84 \times 10^6$	—	—	—	1.89
96	$6.42 \times 10^{-11}$	0.73	$2.12 \times 10^5$	$9.27 \times 10^{-8}$	0.23	$1.05 \times 10^6$	—	—	—	1.31
168	$1.09 \times 10^{-10}$	0.71	$7.33 \times 10^4$	$1.66 \times 10^{-7}$	0.23	$5.56 \times 10^5$	$6.13 \times 10^{-7}$	0.53	$3.26 \times 10^7$	1.79
336	$7.98 \times 10^{-10}$	0.67	$1.60 \times 10^2$	$7.10 \times 10^{-7}$	0.87	$3.55 \times 10^3$	$2.92 \times 10^{-6}$	0.77	$4.20 \times 10^4$	1.58

Table 3

Electrochemical parameters obtained from fitting IL-OL-10 h sample. The unit of Y is ( $\text{S} \cdot \text{s}^n \cdot \text{cm}^{-2}$ ) while the unit of R is ( $\Omega \cdot \text{cm}^2$ ).

Period (h)	$CPE_f$		$R_f$	$CPE_o$		$R_o$	$CPE_i$		$R_i$	$\chi^2 (\times 10^{-3})$
	$Y_f$	$n_f$		$Y_o$	$n_o$		$Y_i$	$n_i$		
5	$2.06 \times 10^{-12}$	0.90	$1.18 \times 10^7$	$1.64 \times 10^{-11}$	0.84	$5.56 \times 10^7$	$2.57 \times 10^{-8}$	0.36	$9.39 \times 10^7$	1.72
12	$1.64 \times 10^{-12}$	0.91	$6.16 \times 10^6$	$8.03 \times 10^{-11}$	0.75	$1.18 \times 10^7$	$5.40 \times 10^{-8}$	0.41	$3.16 \times 10^7$	2.14
24	$3.73 \times 10^{-11}$	0.93	$3.64 \times 10^6$	$7.69 \times 10^{-9}$	0.31	$9.87 \times 10^6$	$2.09 \times 10^{-7}$	0.44	$2.79 \times 10^7$	2.54
96	$4.78 \times 10^{-11}$	0.89	$9.07 \times 10^5$	$1.09 \times 10^{-8}$	0.42	$4.19 \times 10^6$	$1.43 \times 10^{-7}$	0.45	$1.75 \times 10^7$	3.87
168	$1.51 \times 10^{-11}$	0.85	$3.24 \times 10^5$	$1.87 \times 10^{-7}$	0.27	$1.29 \times 10^6$	$8.36 \times 10^{-6}$	0.41	$4.48 \times 10^6$	3.09
336	$6.28 \times 10^{-10}$	0.81	$1.25 \times 10^5$	$1.37 \times 10^{-7}$	0.31	$7.61 \times 10^5$	$2.81 \times 10^{-6}$	0.47	$1.40 \times 10^6$	2.37

Table 4

Electrochemical parameters obtained from fitting IL-OL-24 h sample. The unit of Y is ( $\text{S} \cdot \text{s}^n \cdot \text{cm}^{-2}$ ) while the unit of R is ( $\Omega \cdot \text{cm}^2$ ).

Period (h)	$CPE_f$		$R_f$	$CPE_o$		$R_o$	$CPE_i$		$R_i$	$\chi^2 (\times 10^{-3})$
	$Y_f$	$n_f$		$Y_o$	$n_o$		$Y_i$	$n_i$		
5	$5.56 \times 10^{-12}$	0.91	$3.49 \times 10^7$	$5.91 \times 10^{-10}$	0.82	$6.85 \times 10^7$	$1.96 \times 10^{-7}$	0.42	$8.99 \times 10^7$	2.29
12	$5.66 \times 10^{-12}$	0.91	$3.38 \times 10^7$	$7.98 \times 10^{-11}$	0.77	$4.16 \times 10^7$	$2.46 \times 10^{-7}$	0.32	$7.38 \times 10^7$	3.13
24	$4.54 \times 10^{-12}$	0.93	$1.52 \times 10^7$	$6.03 \times 10^{-10}$	0.76	$3.50 \times 10^7$	$3.52 \times 10^{-7}$	0.36	$6.95 \times 10^7$	1.69
96	$4.90 \times 10^{-11}$	0.92	$1.15 \times 10^7$	$4.40 \times 10^{-10}$	0.21	$2.68 \times 10^7$	$2.27 \times 10^{-7}$	0.57	$4.28 \times 10^7$	2.25
168	$2.21 \times 10^{-11}$	0.89	$7.89 \times 10^6$	$7.81 \times 10^{-9}$	0.47	$8.45 \times 10^6$	$5.53 \times 10^{-7}$	0.41	$1.86 \times 10^7$	0.87
336	$1.09 \times 10^{-10}$	0.88	$6.24 \times 10^6$	$1.66 \times 10^{-8}$	0.23	$3.55 \times 10^6$	$6.13 \times 10^{-7}$	0.53	$1.26 \times 10^7$	1.79

Table 5

Calculated descriptors of ALB and HA molecules using the DFT method.

Molecule	$E_{HOMO}$ (eV)	$E_{LUMO}$ (eV)	$\Delta E$ (eV)	$I$	A	$\chi$	$\eta$	$\Delta N$	S
ALB	-7.5094	-1.0216	6.4878	7.5094	1.0216	4.2655	3.2439	-0.03612	0.3082
HA	-7.6511	0.1336	7.7847	7.6511	-0.1336	3.7587	3.8923	-0.00056	0.2569

### 3.5. Formation mechanism of hybrid films

DFT was utilized to evaluate the active sites responsible for the adsorption of ALB and HA molecules on the surface of IL. Figs. 8 and 9 show the computed FMO structures of both ALB and HA molecules. The chemical reactivity of a reacting molecule would be described by the interaction between its HOMO and LUMO levels [71–74]. The ability of the molecule to donate electrons to electrophilic metal orbitals is described by the high values of  $E_{HOMO}$  while the low value of  $E_{LUMO}$  implies the tendency of a molecule to accept electrons from stronger donating molecules [21]. Accordingly, the high binding ability of the molecule and ions to the metal surface would be described by the higher values of  $E_{HOMO}$  and lower values of  $E_{LUMO}$  [13,31,39]. Based on the DFT results listed in Table 5, the ALB molecule is more reactive than the HA molecule as it possesses a higher  $E_{HOMO}$  value

of (-7.5094 eV) and a lower  $E_{LUMO}$  value of (-1.0216 eV). This would also be described by the low value of the energy gap  $\Delta E = (E_{LUMO} - E_{HOMO})$  for the ALB molecule (~6.49 eV) in comparison to that for HA molecule (~7.78 eV) [31]. Besides, it is well known that the higher reactivity of a molecule would also be described by increasing the softness value (S) or by decreasing the hardness  $\eta$  value [75]. According to the results tabulated in Table 5, ALB would be rigorously reactive than HA. In addition, the interaction of the system metal-surface/organic molecules is subjected to the variation of their electronegativity [33]. This difference in electronegativity trains generally the electron transfer from the organic molecules to the metal surface. The obtained absolute electronegativity values for both tested molecules show that  $\chi$  of ALB is greater than that of HA. Such a result has a significant impact on-trend to attract electrons in the bonding formed between these molecules and the metal surface.

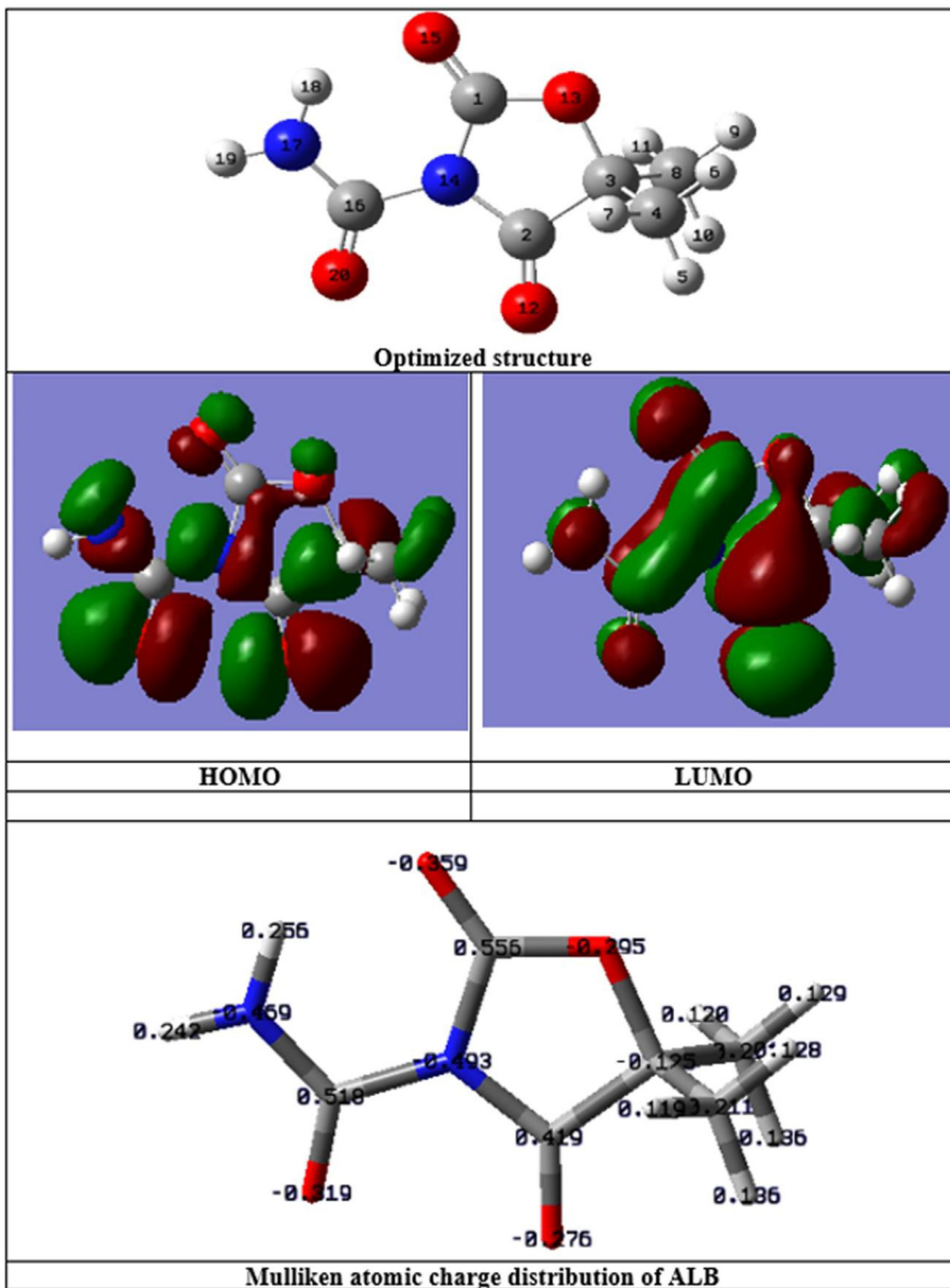


Fig. 8. Optimized structure, the electron density distribution of the HOMO and LUMO orbitals, and Mulliken atomic charge distribution of ALB.

This suggestion is in good agreement with the experimental results obtained above. As the high values of  $\Delta N$  would describe the stability of donor-acceptor, respecting the condition that  $\Delta N$  is less than 3.6, both molecules show a high electron-donating ability, which leads to good coverage of

the metal surface, confirming thus, the electron transfer from the tested organic molecules to the surface. Moreover, from Table 5, the ALB molecule had a higher electron-donating ability than HA which was attributed to the higher number of lone pairs and denticity in ALB due to the presence of the

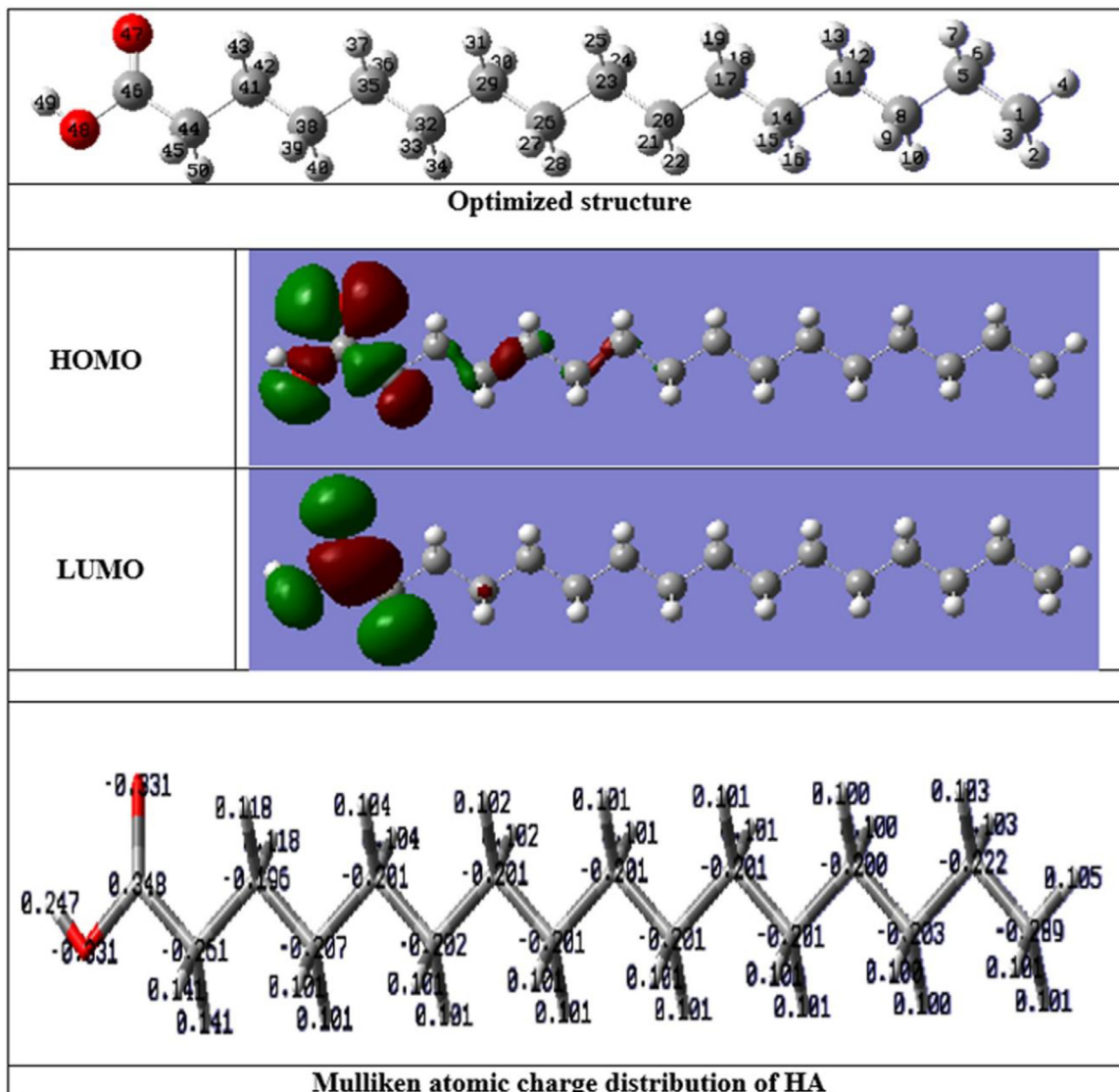


Fig. 9. Optimized structure, the electron density distribution of the HOMO and LUMO orbitals, and Mulliken atomic charge distribution of HA.

peptide group. On the other hand, it is well-known that the adsorption capacity of organic molecules over the metal surface would affect the corrosion inhibition property of the organic molecules [76,77]. In general, the adsorption phenomenon of organic molecules would rely on their physical and chemical characteristics due to several factors related to the functional groups, molecular structure, and electron density, present at the donor atom [78]. First, the  $-\text{COOH}$  group present in HA would form a secondary bond with the IL surface in a process of physisorption [79]. Second, chemisorption may also be involved for the better adsorption capacity where the dissociated  $-\text{COO}^-$  anions form bonds with Mg atoms of the metal surface, leading to the formation of the magnesium carboxylate complex [79]. ALB is involved in the anticorrosion activity as it carries more lone pairs which impede the dissolution of Mg and creating a uniform barrier layer on the IL surface. Here, competitive adsorption between ALB and HA molecules would occur on the surface of IL. Since ALB

molecules have higher reactivity than the HA molecules, as approved by DFT calculations, the surface of IL would be occupied by ALB molecules which hindered to some extent the adsorption of HA molecules. ALB contains more functional groups than that in HA which indicates its strong capability to form a stable barrier monolayer on the IL surface through physical and chemical interactions. This would be occurred by directing the ALB molecules to be adsorbed *via* the lone pairs of electrons of the nitrogen atom of the peptide group ( $\text{CONH}_2$ ), and the oxygen atom of the carbonyl group ( $-\text{COO}$ ), which would form coordinate bonds with IL surface, protecting it from the corrosion [80]. Moreover, with the presence of ALB and HA together, a strong barrier layer could be formed, and the corrosion protection increased because of the uniform, deposition of the OL, which may prevent water molecules and corrosive anions ( $\text{Cl}^-$ ) from penetrating the IL surface through its hydrophobic nature due to the presence of hydrophobic long-chain in HA. The possible bonding be-

tween ALB and HA molecules would also contribute to form a stable OL on the IL, leading to form a stable barrier layer effectively protecting the AZ31 Mg alloy substrate from corrosion. It is interesting to recognize that the better protective properties observed in the case of OL-IL-24 h sample were ascribed to their polarity and the adsorption of OL on the IL through a lone pair of electrons of the ( $\text{CONH}_2$ ), and the oxygen atom of the carbonyl group (-CO) present in solution in higher amounts.

#### 4. Conclusions

In summary, a flowery-like multidimensional structured ALB-HA nanocomposite was successfully made on the defective surface of IL by the chemical doping in the mixed solvent of ethanol and water containing ALB and HA molecules. The flowery flake structures sealed the entire surface of IL helped to suppress the corrosion rate of AZ31 Mg alloy which was ascribed not only to reducing the porosity of IL but also to the strong orbital interactions between ALB and HA which resulted in the formation of a stable organic barrier layer on the surface of IL. Theoretical calculation shows efficient interactions between tested molecules (ALB & HA) and the metal surface thanks to the free-electrons pairs of functional groups existing in these molecules. The results of the theoretical study are in good agreement with those obtained experimentally. The current inexpensive method of producing flowery flakes like organic compounds with a large surface area could find potential catalytic and photocatalytic applications.

#### Declaration of Competing Interest

The authors declare that no conflict of interests.

#### Acknowledgment

This work was supported by the National Research Foundation of Korea (NRF) grant funded by the Korea government (MSIT) (No. NRF-2019R1G1A1099335). This work is supported also by the Mid-Level Researcher National Project of the National Research Foundation (NRF) funded by the Ministry of Science and ICT, Republic of Korea (NRF-2020R1A2C2004192). This research is supported partly by Basic Research Program through the National Research Foundation, Republic of Korea (NRF-2019R1FA1062702).

#### References

- [1] N. Li, Y. Zheng, J. Mater. Sci. Technol. 29 (2013) 489–502.
- [2] S. Jayasathyakawin, M. Ravichandran, N. Baskar, C. Anand Chairman, R. Balasundaram, Mater. Today Proceed. 27 (2020) 909–913.
- [3] M. Esmaily, J.E. Svensson, S. Fajardo, N. Birbilis, G.S. Frankel, S. Virtanen, R. Arrabal, S. Thomas, L.G. Johansson, Prog. Mater. Sci. 89 (2017) 92–193.
- [4] T. Narayanan, P. Song, M. Lee, Prog. Mater. Sci. 60 (2014) 1–71.
- [5] F. Witte, J. Fischer, J. Nellesen, C. Vogt, J. Vogt, T. Donath, F. Beckmann, Acta Biomater. 6 (2010) 1792–1799.
- [6] J.H. Gao, X.Y. Shi, B. Yang, S.S. Hou, E.C. Meng, F.X. Guan, S.K. Guan, J. Mater. Sci. Mater. Med. 22 (7) (2011) 1681–1687.
- [7] R.G. Hu, S. Zhang, J.F. Bu, C.J. Lin, G.L. Song, Prog. Org. Coat. 73 (2012) 129–141.
- [8] X.J. Cui, C.H. Liu, R.S. Yang, Q.S. Fu, X.Z. Lin, M. Gong, Corros. Sci. 76 (2013) 474–485.
- [9] S. Pommiers, J. Frayret, A. Castetbon, M. Potin-Gautier, Corros. Sci. 84 (2014) 135–146.
- [10] T. Ishizaki, J. Hieda, N. Saito, O. Takai, Electrochim. Acta 55 (2010) 7094–7101.
- [11] M. Kaseem, T. Hussain, Z.U. Rehman, Y.G. Ko, J. Alloys Compd. 853 (2020) 157036.
- [12] M. Kaseem, S. Fatimah, N. Nashrah, Y.G. Ko, Prog. Mater. Sci. 117 (2021) 100735.
- [13] M. Kaseem, T. Hussain, S.H. Baek, Y.G. Ko, Mater. Des. 193 (2020) 108823.
- [14] S.S. Farhadi, M. Aliofkhazraei, Gh. Barati Darband, A. Abolhasani, A. Sabour Rouhaghdam, J. Magnes. Alloys 5 (2017) 210–216.
- [15] W. Zhang, Y. Yu, P. Zhang, J. Magnes. Alloys doi:10.1016/j.jma.2021.01.003
- [16] Z. Ur Rehman, D. Choi, J. Magnes. Alloys 7 (2019) 555–565.
- [17] M. Kaseem, K. Ramachandraiah, S. Hossain, B. Dikici, Nanomaterials 11 (2) (2021) 536.
- [18] M. Kaseem, T. Hussain, Z.U. Rehman, M.J. Banisalman, Y.G. Ko, Surf. Coat. Technol. 399 (2020) 126200.
- [19] L. Zhao, Q. Liu, J. Wang, W. Yang, L. Liu, Corros. Sci. 80 (2014) 177–183.
- [20] K. Aramaki, T. Shimura, Corros. Sci. 46 (2004) 313–328.
- [21] A. Ulman, Chem. Rev. 96 (1996) 1533–1554.
- [22] Y. Liu, Z. Yu, S. Zhou, L. Wu, Appl. Surf. Sci. 252 (2006) 3818–3827.
- [23] X.J. Cui, X.Z. Lin, C.H. Liu, R.S. Yang, X.W. Zheng, M. Gong, Corros. Sci. 90 (2015) 402–412.
- [24] Z. Wang, Q. Li, Z. She, F. Chen, L. Li, X. Zhang, P. Zhang, Appl. Surf. Sci. 271 (2013) 182–192.
- [25] P. Wang, D. Zhang, R. Qiu, Y. Wan, J. Wu, Corros. Sci. 80 (2014) 366–373.
- [26] B.T. Qian, Z.Q. Shen, Langmuir 21 (2005) 9007–9009.
- [27] M. Guo, Z. Kang, W. Li, J. Zhang, Surf. Coat. Technol. 239 (2014) 227–232.
- [28] S. Ding, N. Zhang, Z. Lyu, W. Zhu, Y.C. Chang, X. Hu, D. Du, Y. Lin, Mater. Today. 10.1016/j.mattod.2020.11.015
- [29] M. Kaseem, Y.G. Ko, Compos. Part B 176 (2019) 107225.
- [30] M. Kaseem, Y.G. Ko, Compos. Part B Eng. 204 (2021) 108490.
- [31] M. Kaseem, T. Hussain, Z. Ur Rehman, H.W. Yang, B. Dikici, Y.G. Ko, Chem. Eng. J. 420 (2021) 129737.
- [32] M.E. Belghiti, S. Echihi, A. Dafali, Y. Karzazi, M. Bakasse, H. ElalaouiElabdallaoui, L.O. Olasunkanmi, E.E. Ebenso, M. Tabayou, Appl. Surf. Sci. 491 (2019) 707–722.
- [33] M.E. Belghiti, Y. El Ouadi, A. Elmelouky, H. Outada, Y. Karzazi, M. Bakasse, C. Jama, F. Bentiss, A. Dafali, Surf. Interfaces 21 (2020) 100692.
- [34] A. Berrissoul, E. Loukili, N. Mechbal, F. Benhiba, A. Guenbour, B. Dikici, A. Zarrouk, A. Dafali, J. Colloid Interface Sci. 580 (2020) 740–752.
- [35] R.G. Pearson, Inorg. Chem. 27 (1988) 734–740.
- [36] R.O. Hussein, X. Nie, D.O. Northwood, Electrochim. Acta 112 (2013) 111–119.
- [37] A.B. Rogov, A. Matthews, A. Yerokhin, Electrochim. Acta 317 (2019) 221–231.
- [38] J. Liang, P.B. Srinivasan, C. Blawert, M. Stormer, W. Dietzel, Electrochim. Acta 54 (14) (2009) 3842–3850.
- [39] T. Hussain, M. Kaseem, Y.G. Ko, Corros. Sci. 170 (2020) 108663.
- [40] L. Chen, W. Feng, X. Zhou, K. Qiu, Y. Miao, Q. Zhang, M. Qin, L. Li, Y. Zhang, C. He, RSC Adv. 6 (2016) 13040–13049.
- [41] E. Mavropoulos, A.M. Costa, L.T. Costa, C.A. Achete, A. Mello, J.M. Granjeiro, A.M. Rossi, Colloids Surf. B Biointerfaces 83 (2011) 1–9.

- [42] M.C. Coen, R. Lehman, P. Groning, M. Bielmann, C. Galli, L. Schlapbach, *J. Colloid Interface Sci.* 233 (2001) 180–189.
- [43] Z. Chang, H. Yan, J. Tian, H. Pan, H. Pu, *Polym. Degrad. Stab.* 138 (2017) 98–105.
- [44] M. Kulkarni, A. Mazare, J. park, E. Gongadze, M.S. Killian, S. Kralj, K.V.D. Mark, A. Iglic, P. Schmuki, *Acta Biomater.* 45 (2016) 357–366.
- [45] F. Mumtaz, C.S. Chen, H.K. Zhu, M. Atif, Y.M. Wang, Chin. J. Polym. Sci. 36 (2018) 1328–1341.
- [46] L. Yu, J. Cao, Y. Cheng, *Surf. Coat. Technol.* 276 (2015) 266–278.
- [47] Y. Gu, S. Bandopadhyay, C.F. Chen, Y. Guo, C. Ning, *J. Alloys Compd.* 543 (2012) 109–117.
- [48] S.V. Gnedekov, S.L. Sinebryukhov, D.V. Mashtalyar, K.V. Nadaraia, A.S. Gnedekov, V.M. Bouznik, *Corros. Sci.* 111 (2016) 175–185.
- [49] H.S. Ryu, J. Ryu, D.S. Park, S.H. Hong, *J. Electrochem. Soc.* 158 (2) (2011) C23–C28.
- [50] S. Hariprasad, S. Gowtham, S. Arun, M. Ashok, N. Rameshbabu, *J. Alloys Compd.* 722 (2017) 698–715.
- [51] S.V. Gnedekov, S.L. Sinebryukhov, D.V. Mashtalyar, K.V. Nadaraia, D.P. Kiryukhin, G.A. Kichigina, P.P. Kushch, V.M. Buznik, *Surf. Coat. Technol.* 346 (2018) 53–62.
- [52] S. Fatimah, F. Khoerunnisa, J. Kwon, Y. Kim, Y. Ko, *Surf. Coat. Technol.* 360 (2019) 56–63.
- [53] N. Kamiyama, G. Panomswan, E. Yamamoto, T. Sudare, N. Saito, T. Ishizaki, *Surf. Coat. Technol.* 286 (2016) 172–177.
- [54] D. Zhang, Y. Gou, Y. Liu, X. Guo, *Surf. Coat. Technol.* 236 (2013) 52–57.
- [55] L. Wu, D. Yang, G. Zhang, Z. Zhang, S. Zhang, A. Tang, F. Pan, *Appl. Surf. Sci.* 431 (2018) 177–186.
- [56] D.K. Ivanou, M. Starykevich, A.D. Lisenkov, M.L. Zheludkevich, H.B. Xue, S.V. Lamaka, M.G.S. Ferreira, *Corros. Sci.* 73 (2013) 300–308.
- [57] T. Ishizaki, Y. Masuda, M. Sakamoto, *Langmuir* 27 (2011) 4780–4788.
- [58] D.V. Mashtalyar, K.V. Nadaraia, S.L. Sinebryukhov, S.V. Gnedekov, *J. Mater. Sci. Technol.* 33 (2017) 661–667.
- [59] G. Zhang, L. Wu, A. Tang, B. Weng, A. Atrens, S. Ma, L. Liu, F. Pan, *RSC Adv.* 8 (2018) 2248–2259.
- [60] J. Liang, P.B. Srinivasan, C. Blawert, W. Dietzel, *Corros. Sci.* 51 (2009) 2483–2492.
- [61] S.V. Gnedekov, S.L. Sinebryukhov, V.I. Sergienko, *Russ. J. Electrochem.* 42 (2006) 197–211.
- [62] A. López-Ortega, J.L. Arana, E. Rodríguez, R. Bayón, *Corros. Sci.* 143 (2018) 258–280.
- [63] M. Mohedano, C. Blawert, M.L. Zheludkevich, *Mater. Des.* 86 (2015) 735–744.
- [64] B. Mingo, R. Arrabal, M. Mohedano, Y. Lilamazares, A. Yerokhin, A. Pardo, *Appl. Surf. Sci.* 433 (2018) 653–667.
- [65] G. Zhang, L. Wu, A. Tang, Y. Ma, G-Ling Song, D. Zheng, B. Jiang, A. Atrens, F. Pan, *Corros. Sci.* 139 (2018) 370–382.
- [66] M. Kaseem, T. Hussain, Y.G. Ko, *J. Alloys Compd.* 822 (2020) 1533566.
- [67] V. Palanivel, D. Zhu, W.J. van Ooij, *Prog. Org. Coat.* 47 (2003) 384–392.
- [68] T. Zehra, M. Kaseem, S. Hossain, Y.G. Ko, *Metals* 11 (8) (2021) 1182 (Basel), doi:10.3390/met11081182.
- [69] Z. Yao, Z. Jiang, S. Xin, X. Sun, X. Wu, *Electrochim. Acta* 50 (2005) 3273–3279.
- [70] D. He, G. Li, D. Shen, C. Guo, H. Ma, J. Cai, *Vacuum* 107 (2014) 99–102.
- [71] G. Gece, *Corros. Sci.* 50 (2008) 2981–2992.
- [72] M. Lebrini, M. Lagrene, M. Traisnel, L. Gengembre, H. Vezin, F. Bentiss, *Appl. Surf. Sci.* 253 (2007) 9267–9276.
- [73] K. Zhang, B. Xu, W. Yang, X. Yin, Y. Liu, Y. Chen, *Corros. Sci.* 90 (2015) 284–295.
- [74] Z. Hu, Y. Meng, X. Ma, H. Zhu, J. Li, C. Li, D. Cao, *Corros. Sci.* 112 (2016) 563–575.
- [75] M. Finsgar, A. Lesar, A. Kokalj, I. Milosev, *Electrochim. Acta* 53 (2008) 8287–8297.
- [76] A.A. Al-Amiry, F.A. Binti Kassim, A.A.H. Kadhum, A.B. Mohamad, *Sci. Rep.* 6 (2016) 19890.
- [77] M.P. Rai, A. Khanra, S. Rai, M. Srivastava, R. Prakash, *J. Mol. Liq.* 266 (2018) 279–290.
- [78] I.M. Mousaa, H. Radi, *Corros. Eng. Sci. Technol.* 52 (2017) 547–556.
- [79] R.R. Sahoo, S.K. Biswas, *J. Colloid Interface Sci.* 333 (2009) 707–718.
- [80] K. Cherrak, M.E. Belghiti, A. Berrissoul, M. El Massaoudi, M. El Faydy, M. Taleb, S. Radi, A. Zarrouk, A. Dafali, *Surf. Interfaces*, 20